Mon. Not. R. Astron. Soc. **000**, 1–15 (2012) Printed 6 May 2012 (MN LaTeX style file v2.2)

From Bipolar to Elliptical: Simulating the Morphological Evolution of Planetary Nebulae

M. Huarte-Espinosa[1⋆], A. Frank[1], B. Balick[2], E. G. Blackman[1], O. De Marco[3,4], J. H. Kastne

[1] *Department of Physics and Astronomy, University of Rochester, 600 Wilson Boulevard, Rochester, NY, 14627-0171*
[2] *Department of Astronomy, University of Washington, Seattle, WA 98195*
[3] *Department of Astrophysics, American Museum of Natural History, Central Park West at 79th Street, New York, NY 10024*
[4] *Department of Physics, Macquarie University, Sydney NSW 2109, Australia*
[5] *Rochester Institute of Technology, 54 Lomb Memorial Drive, Rochester, NY 14623, USA*
[6] *NASA/JPL, 4800 Oak Grove Drive, Pasadena, CA 1109, USA*

Received 6 May 2012

ABSTRACT

In this paper we model the evolution of PrePlanetary Nebula (PPN) and Planetary Nebula (PN) morphologies as a function of nebular age. The aim of the work is to understand if shape transitions from one evolutionary phase to the other can be driven by changes in the parameters of the mass-loss from the central star. We carry out 2.5D hydrodynamical simulations of mass-loss at the end stages of stellar evolution for intermediate mass stars. Changes in wind velocity, mass-loss rate and mass-loss geometry are tracked. We focus on the transition from mass-loss dominated by a short duration jet flow (driven during the PPN phase) to mass-loss driven by a spherical fast wind (produced by the central star of the PN). Our results show that while jet driven nebulae can be expected to be dominated by bipolar morphologies, systems that begin with a jet but are followed by a spherical fast wind will evolve into elliptical objects.

Systems that begin with an aspherical AGB wind evolve into butterfly shaped nebula with, or without, a jet phase. In addition, our models show that spherical nebulae are highly unlikely to derive from either bipolar PPN or elliptical PN over relevant time scales. The morphological transitions seen in our simulations may however provide insight into the driving mechanisms of both PPN and PN as point to evolutionary changes in the central engine.

Key words: stars: AGB and post-AGB – (ISM:) planetary nebulae: general – stars: winds, outflows – hydrodynamics – radiative transfer – methods: numerical

1 INTRODUCTION

Planetary Nebulae (PN) expand at a few $10\,\mathrm{km\,s^{-1}}$ away from evolved intermediate-mass stars (with main sequence progenitor masses ~ 1–$8\,\mathrm{M_{\odot}}$). These nebulae exhibit a rich variety of morphologies with the main categories being spherical, elliptical and bipolar (for a review see Balick & Frank 2002). Spherical PN have been explained by time-dependent interacting stellar wind models (ISW; Kwok, Purton, & Fitzgerald 1978) that describe the nebula as the collision of a fast ($\sim 1000\,\mathrm{km\,s^{-1}}$) tenuous (between about 10^{-8} and 10^{-7} $\mathrm{M_{\odot}\,yr^{-1}}$) stellar wind driven by the hot central star of PN (CSPN) with a dusty slow ($\sim 10\,\mathrm{km\,s^{-1}}$) dense ($\sim 10^{-4}\,\mathrm{M_{\odot}\,yr^{-1}}$) wind, or circumstellar envelope, ejected during the earlier AGB phase. The nebulae are thus formed when the fast wind catches up with the AGB wind, driving a shocked shell through it.

The formation of bipolar PN and jets has been addressed by generalized ISW models (GISM) in which the ejected AGB envelope is characterized by either a toroidal density distribution or an aspherical velocity field (Kahn & West 1985; Balick 1987; Icke 1988; Huggins 2007; Frank & Mellema 1994; Icke 1988; Icke, Preston, & Balick, 1989; Mellema, Eulderink, & Icke, 1991; Icke, Balick, & Frank, 1992; Frank & Mellema 1994; Dwarkadas, Chevalier, & Blondin, 1996). In some of these models, asymmetries in AGB envelopes develop as a result of a binary stellar system, in which an AGB star interacts with a companion (García-Arredondo & Frank 2004; Edgar et al. 2008), or an AGB star and a companion share a common envelope evolution (Iben 1991; Livio 1993; Soker 1997; Sandquist et al. 1998; Soker 1998, and references therein; De Marco et al. 2003; Nordhaus et al. 2007; Passy et al. 2012). Note, however, that

⋆ E-mail: martinhe@pas.rochester.edu

AGB envelopes generally show spherical shapes (Bujarrabal & Alcolea 1991; Kahane & Jura 1994; Stanek et al. 1995; Groenewegen 1996). Some AGB observations show seeds of asymmetry.

The original GISW model (see e.g. Balick & Frank 2002) assumed a spherical fast wind driven from the CSPN expanding into an aspherical AGB wind. While these models were able to generate hot, low density jet flows via shock focusing at the inner shock, they were less successful at recovering dense colder jets like those seen in YSOs. Since many PPN and young PN show evidence for such narrow jets, Sahai & Trauger (1998) suggested that collimated PN flows created at, or near, the central engine were the real drivers of early PN morphology. Such jet formation has been proposed as a natural consequence of interacting binary evolution (Lee & Sahai 2003, 2004; Akashi & Soker 2008; Lee et al. 2009). Lee & Sahai (2003) carried out numerical simulations and synthetic observations of a jet (or collimated fast wind) interacting with a spherical AGB wind. They found that both the dynamics and emission of PPN, and young PN, shells depend on the velocity and geometry of the jet. Using a similar approach Akashi & Soker (2008) modeled the effect of short-duration jets expanding into a spherical, slow AGB wind on the observed shape of evolved PN. The simulations of Akashi & Soker (2008) covered timescales about an order of magnitude longer than the ones of Lee & Sahai (2003). Akashi & Soker (2008) found that the AGB mass-loss history also has a profound influence on the nebular structure, and that the head of the lobes move sufficiently fast to excite some visible emission lines (see Lee & Sahai 2003 for detailed results of optical forbidden line emission which is excited at the heads of the lobes during the PPN phase). These studies did not address the question as to how the older, AGB spherical outflows would respond to “fresh”, collimated outflows from the PN central engine.

In this paper we focus on a theoretical exploration of the role that changing mass-loss geometries from the central engine can play in driving changes in nebular morphology. If PPN drive collimated outflows off the central engine but PN drive primarily spherical outflows then how will the nebula respond as it expands? The aim is to understand how nebulae change form as their hydrodynamic driving changes. Such process is of interest because it might help to understand the history of the central engine which may be a single star, a recently processed common envelope system or a binary with an accretion disk. Thus there is the hope that one might be able to use morphological clues in an individual nebula to recover something of the history of the central object in terms of its mass-loss and the conditions which govern it.

We note that there is a broader observational motivation for this study. The classifications of PPN and PN by morphological type appear to show significant statistical differences. The general trends indicate that (i) around 70 to 90% of PPN and young PN are bipolar or more complex (Sahai & Trauger 1998; Sahai et al. 2011), (ii) about 20% of mature PN are round, 70% are elliptical and about 10% are bipolar (see Miszalski et al. 2009a; Parker et al. 2006; Lagadec et al. 2011; the Planetary Nebula Image Catalog of Bruce Balick[1] and references therein). There are however considerable uncertainties in these classifications, e.g. (i) telescope resolution limitations; (ii) stellar population selection effects; (iii) differences in nebular class definitions (for example ring-like nebulae that are actually toroids included in spherical morphological classes); (iv) the well-established correlation between PN morphology and the progenitors' mass, i.e., bipolar and ring-like PN generally found at lower galactic scale heights, characteristic of higher-mass progenitors (see e.g. Corradi & Schwarz 1995; Kastner et al. 1996; Manchado et al. 2011). These factors, along with the fact that most attempts to classify PN by morphological type do not consider the ages of the nebulae (but see Sahai & Trauger 1998; Sahai et al. 2011 for specific studies on young PN), complicate the interpretation of temporal changes in nebular morphology.

If the imbalance between PPN and PN statistics holds up under further scrutiny then it implies that some objects may undergo a shape transformation as they expand. In particular, one can imagine a scenario in which bipolar PPN hydrodynamically transform into elliptical or rounder PN. Such a transformation could be caused by different nebular driving mechanisms during the early and late nebular evolutionary phases.

Irrespective of issues of observational statistics, in this paper we take on the issue of morphological changes in PPN/PN from a theoretical perspective. Starting from a set of basic physical ingredients and using simulations, we aim to understand how shape transitions might occur during the evolution of an individual post-AGB system and how such morphological transitions depend on the parameters of the mass-loss process of the central star. The morphological evolution of single sources should be studied from first principles to better inform the interpretation of observations. Thus we consider the influence of an initial collimated jet phase during the PPN and its effect on the previously deposited circumstellar AGB wind. The jet phase is followed by a classical fast wind with a spherical geometry. Different distributions of the AGB wind's velocity and density are explored as are other parameters for the jet/wind interactions. Our choices for initial and boundary conditions are based on a reasonable balance between observational expectations and computational expediency. We note Soker (1990) has studied PN ansae using a similar wind/jet sequence, but here we carry out a more extensive study and explore a range of parameters across both PPN and PN evolution.

This paper is organized as follows: in section 2 we describe the methodology and numerical code used in the study, as well as our model and implementation of the AGB wind and post-AGB stellar outflows. The results of the simulations are presented in section 3. In section 4 we compare our results with the general trends found by observations by means of synthetic emission maps and discuss how the results bear on issues of PN shaping. Conclusions are presented in section 5.

[1] http://www.astro.washington.edu/users/balick/PNIC/

2 MODEL AND METHODOLOGY

We carry out a set of Eulerian-grid numerical simulations to follow the interaction of collimated jets and winds. The initial and inflow conditions are meant to model nebular evolution from the AGB to the mature PN phases. Wind dynamics are modeled and followed in 2.5 dimensions (cylindrical symmetry) using the equations of radiation hydrodynamics. The effects of optically thin cooling have been included using the cooling tables of Dalgarno & McCray (1972). We note that radiative cooling will play an important role in the shocks driven by the jet and also in the "rim" of swept up AGB material driven by the fast wind. Because of its high velocity the shocked fast wind should form a high temperature "hot bubble", $T_{\rm hb} \sim 10^7$ K, that will not cool effectively during the evolution of the PN. Observations have established, however, that only certain PN show such hot bubble emission and that the temperature is usually lower, by factors of order 10 to 100, than that predicted by the jump conditions (e.g. Kastner et al. 2008, and references therein).

The hydrodynamic equations are solved with the adaptive mesh refinement (AMR) numerical code AstroBEAR1.0[2]. In particular the Euler equations with cooling source terms are solved using a second-order MUSCL-Hancock shock capturing scheme and Marquina flux functions (Cunningham et al. 2009). While AstroBEAR1.0 is able to solve the equations of magnetohydrodynamics (MHD) and to compute several microphysical processes, such as gas self-gravity and heat conduction, we do not consider these processes in the present study. We justify these omissions at present on the basis that jets are likely formed via MHD processes at the central engine, but magnetic fields are not likely to dominate global morphologies at nebular scales (Hartigan et al. 2007).

The numerical domain of the simulations is 1 pc on each side. We use cylindrical coordinates (r, z) in a box that includes explicit calculations of the pole to avoid numerical issues there[3]. Thus our simulation extends from $-r_{max}$ to r_{max}, where r_{max} =0.5pc. Extrapolation, or outflow, boundary conditions are used at $r = \pm 0.5$ pc (above and below the z axis) and at $z = 1$ pc. Reflective boundary conditions are imposed at the "equator" of the system ($z = 0$). We consider cells with radii $R < r_w$, where $r_w \sim 6000$ AU, to be the "nozzle" of the jets/wind and we apply inflow boundary conditions there (see below).

A coarse grid of 128×128 cells is employed along with two levels of AMR refinement, each increasing the resolution by a factor of 2. Thus the simulations attain a maximum resolution of 512×512 with a $\Delta X_{min} \sim 403$ AU. Typical simulation flow times are of order 13000 yr which is about ten times longer than previous simulations of PN evolution (e.g. compare with Lee & Sahai 2003, 2004; Lee et al. 2009; Akashi & Soker 2008). We use BlueHive[4], an IBM parallel cluster maintained at the Center for Integrated Research Computing of the University of Rochester, to run simulations for about 20 hrs, using 16 processors.

2.1 Outflow Phases

Three outflow episodes are considered in the simulations. The first one, the "AGB wind", constitutes AGB initial conditions (e.g. Knapp & Morris 1985) set on the entire computational grid. These conditions are such that the edge of the AGB envelope is located outside our computational domain. Our AGB wind/circumstellar environment has an isotropic radial velocity field of v_{AGB} =10 km s^{-1} and a mass-loss rate of $\dot{M}_{AGB} = 1\times10^{-5}$ M$_\odot$ yr^{-1}. These values are representative of observed AGB wind properties (Hrivnak et al. 1989; Bujarrabal et al. 2001). The AGB wind is set up with a uniform temperature of 500 K which best represents the inner region of the envelope. We would actually expect a temperature gradient, with the outer temperature being colder, however this simplification does not affect the current model.

The second outflow phase, the "jet", begins immediately upon the initiation of the simulation. A collimated jet, with an opening angle of zero degrees, is injected at cells with radii $< r_w$ ($\sim$6000 AU). The jet's velocity, temperature and mass-loss rate are 200 km s^{-1}, 500 K and $\dot{M}_j = 5\times10^{-6}$ M$_\odot$ yr^{-1} (= 0.5 $\dot{M}_{AGB}$), respectively. The jet is active for approximately 100 yr which is about 1% of the average total simulation run time. The launch and collimation of our jets are assumed to occur in the "central engine" (likely a binary or strongly magnetized stellar winds[5]) located at sub-resolution scales of order 10 AU. The jet injection timescale is representative of expansion times (which are of order 500 yr) of some PPN and PN which can be directly imaged (e.g. see the PPN jet sample in Huggins 2007, and references therein). Jet mass-loss rates are not well characterized so we have used an intermediate value (yet higher than those used in previous simulations, e.g. see Lee et al. 2009, and references therein) between the AGB and CSPN evolutionary stages, consistent with both momentum excesses observed in PPN flows (Bujarrabal et al. 2001) and the observations of A 63 carried out by Mitchell et al. (2007).

The third outflow phase we consider, the "fast wind", is a standard central stellar fast wind (Kwok et al. 1978) with a spherical velocity field continuously injected into the computational domain through the nozzle. In our three-phase models the spherical wind remains active throughout the remainder of the simulation after the jet is turned off. The fast wind has a mass-loss rate that decreases in time over $\sim 10^4$ yr from 5×10^{-7} to 5×10^{-9} M$_\odot$ yr^{-1}, following the results of Perinotto et al. (2004, and references therein). Once $\dot{M}$ reaches 5×10^{-9} M$_\odot$ yr^{-1} it remains constant at that rate until the end of the simulation. Simultaneously, the fast wind increases in speed from 200 to 2000 km s^{-1} in a manner that conserves wind ram pressure. This set of final fast wind conditions was chosen for computational expediency. Gas temperature in the wind at the nozzle is set such that the wind

[2] http://bearclaw.pas.rochester.edu/trac/astrobear/wiki
[3] We moved the bottom grid boundary away form the nebular pole. Cells along this axis were evolved as grid cells, not as boundary (ghost) ones, by solving the equations of hydrodynamics. Hence we do not introduce any known numerical artifacts related to reflective boundaries on those cells.
[4] https://www.rochester.edu/its/web/wiki/crc/index.php/BlueHive_Cluster

[5] We do not delve here on the actual physical causes of jets and other phenomena. We merely study the effect of sequences of plausible events on the PN morphology.

maintains a constant Mach number of 20 (again, for computational expediency; the model results are not sensitive to this).

We now review the suite of simulations carried out for the study. To isolate the effect of the jet we ran a series of two-phase simulations in which only the jet is launched into the AGB wind (Models 1 and 4, see Table 1). After the jet episode ends in these models no further gas is injected into the grid. Also, the simulations represented by Models 2, 2*, 2b, 2b*, 5 and 7 are two-phase models in which the fast wind is injected directly into the AGB wind. The simulations represented by Models 3, 3* and 6 are three-episode scenarios in which the fast wind is injected immediately after the jet, at time $t \sim 100\,yr$ (see Table 1). The simulation represented by Model 8 is almost the same as Model 3, except that the former has a wind-quiescent interlude that lasts $\sim 400\,\mathrm{yr}$ between the jet and the fast wind episodes. The interlude represents an arbitrary timescale of order 4 times the jet's duty cycle (or active time) chosen to be long enough to allow the jet driven cavity to evolve but short enough to be consistent with PPN/CSPN transition timescales.

All simulations and their parameters, including the additional models that we present below, are summarized in Table 1. Evolutionary profiles of the outflow conditions are presented in Figure 1. We note again that the initial conditions are those of the AGB wind and set throughout the computational domain, whereas the conditions of both jet and fast wind episodes are set only on the gas located inside the nozzle ($R < r_w$, see above).

2.2 Ionization front

As the central star evolves from the AGB to the proto-white dwarf stages its surface temperature dramatically and rapidly increases and so does its flux of ionizing UV photons (Balick 1987; Hollenbach & Tielens 1997; Perinotto et al. 2004). Thus an ionization front will be driven away from the star into the surrounding circumstellar medium. Upon ionization the former neutral AGB envelope will be heated from temperatures of order $T_{neb} \sim 10\,K$ to $T_{neb} \sim 10^4\,K$.

The numerical description of ionization fronts with AMR requires the implementation of sophisticated methods for radiative transfer. Efforts are currently underway to incorporate such methods into AstroBEAR2.0. In the current study we have implemented a simplified approximation which accounts for the thermal effect of ionization. When the fast stellar wind reaches a velocity of $2000\,\mathrm{km\,s^{-1}}$ we increase the temperature of cold gas ($\lesssim$500 K) to 10000 K. This temperature increase is imposed instantaneously across the entire computational domain. In this way we assume that the nebula is density bounded and that the ionization front is R-type[6] (see Giuliani 1981, and references therein), sweeping across the nebular domain in a timescale $t_i \sim R/c$ that is very short compared with the hydrodynamical evolution timescale $t_h \sim R/v_w$ (where R, c and v_w are the radius of the nebula, the speed of light and the speed of the fast wind, respectively). In reality, however, ionization will not be as effective in the equatorial plane as towards the poles.

[6] In a R-type ionization front gas is advected at supersonic velocities and exhausts at a slightly lower, but still supersonic, velocity.

Simulations that include this parametrization of ionization front passage are marked with an asterisk. For example, other than including the ionization-generated temperature increase, Model 1* is identical to Model 1, Model 2* is identical to Model 2, etc. (see Table 1). While this method is crude it allows us to test the potential of the pressure generated via ionization to change the evolution of the overall nebular morphology at late states in its evolution.

2.3 Additional models

For completeness we have also chosen to carry out a series of GISW models in which bipolar nebular morphologies are expected to form in the PN phase (rather than through jets in the PPN phase). The GISW model relies on pole to equator density contrasts in an aspherical, toroidally shaped AGB envelope. Since toroidal AGB density distributions have been adopted in GISW models before (e.g. see Frank & Mellema 1994) we have decided to run a series of models that include such density gradients as initial AGB wind conditions. Specifically, the AGB (ambient/circumstellar) density distribution in Models 4, 5 and 6 is the AGB aspherical density distribution used by Icke et al. (1992, but see also references therein) and Frank & Mellema (1994), where

$$\rho_{torus} = \frac{\rho_{AGB}}{F(\theta)} \left(\frac{r_w}{r}\right)^2, \quad (1)$$

$$F(\theta) = 1 - \alpha \left(\frac{e^{\beta cos(2\theta) - \beta - 1}}{e^{-2\beta} - 1} \right), \quad (2)$$

and $\rho_{AGB} = \dot{M}_{AGB}/\ (4\pi v_{AGB} r^2)$.

This functional form produces a well characterized pole to equator density contrast. For example with $\alpha = 0.5$ and $\beta = 1$ the above expressions introduce a pole to equator density contrast of 0.5 in the AGB wind. We have chosen these values in our study as they have been shown to produce butterfly type bipolar morphologies in pure GISW models (Frank & Mellema 1994).

Model 4 is a two phase simulation and follows the interaction only of the jet with the toroidal AGB wind. Model 5 is also a two phase simulation but it follows only the fast wind interacting with the toroidal AGB wind. Model 6 is a three phase simulation tracking the jet followed by the fast wind interacting with the (preexisting) toroidal AGB wind (see Table 1).

Finally, we explore the role of velocity gradients in the AGB wind. We have carried out a simulation in Model 7 in which $V_{AGB} = V(\theta) = f(r, z) * V_o$ where the constant radial velocity field V_o is multiplied by the function

$$f(r, z) = 1 + e^{-tan^{-1}(|r/z|)^2/0.3^2}, \quad (3)$$

which results in a latitudinal decreasing expansion velocity, with a polar-to-equatorial contrast ratio of 2. A continuous fast wind is then driven into this aspherical AGB wind. As we shall see in the next section such a velocity gradient does not greatly affect the morphology of the resulting nebula.

3 RESULTS

The results of our simulations are presented via logarithmic false color gray scale maps of the gas density **with overlaid**

Table 1. Simulations and parameters.

Simulation name	AGB wind distribution	Jet duration [$\times 100$ yr]	Fast wind duration [$\times 1000$ yr]	Fast wind max. speed [$\times 1000\,\mathrm{km\,s^{-1}}$]	Ionization front passage
Model 1	spherical	1	0.0	...	n
Model 1*	spherical	1	0.0	...	y
Model 2	spherical	0	13.0	2	n
Model 2*	spherical	0	13.0	2	y
Model 2b	spherical	0	16.3	1	n
Model 2b*	spherical	0	16.3	1	y
Model 3	spherical	1	10.7	2	n
Model 3*	spherical	1	10.7	2	y
Model 4	toroidal ρ	1	0.0	...	n
Model 5	toroidal ρ	0	3.8	2	n
Model 6	toroidal ρ	1	6.0^a	2	n
Model 7	aspherical $\vec{v}$	0	13.0	2	n
Model 8[b]	spherical	1	18.0	2	n

[a] This time is shorter than the one of Model 3 (10.7 kyr) because the toroidal AGB wind in this model funnels the nebula's lobe and thus it reaches the computational domain's boundary faster than the lobe in Model 3.
[b] Model 8 includes a relaxation interlude of ~ 400 yr between the jet and the wind episodes, and a computational domain of $2\,\mathrm{pc}^2$, instead of $1\,\mathrm{pc}^2$ as in other simulations.

velocity vectors in Figures 2–5. Panels in these figures are arranged such that **columns correspond to different simulations and rows show time increasing from top to bottom.**

3.1 Structure within spherical AGB winds

Jet Models: In figure 2, left column, we show the results of Model 1, in which a short collimated jet phase is driven into a spherical AGB wind envelope. The figure shows the jet driving a bow shock which bounds a narrow-waisted cavity. The cavity wall is defined by a thin dense "rim" and its bipolar geometry persists for the entire duration of the simulation. The lateral width of the lobe is the result of the thermal pressure within the cavity as shocked material is forced laterally out of the region of the jet head. Thus the lobe's width-to-length ratio is determined by the sound speed in the AGB shell and the speed of the jet head. We note that the cooling time of the post-shock gas, $t_c \sim T/(n\Lambda(T))$, where $\Lambda(T)$ is the cooling function (Dalgarno & McCray 1972), is short relative to the hydrodynamic time (which is the ratio of the computational domain length over the gas sound speed). Thus all post-shock flows in this simulation are relatively isothermal.

After about 3500 yr, the cavity lobe develops a narrow waist. This timescale is of order the expansion time of mature, but not old, PN. The pinch at the waist is the result of the higher density (and, therefore, higher ram pressure) of the AGB shell at small radii. In section 4.1 we analyze the evolution of the aspect ratio of some of our model nebulae. Here we note the aspect ratio of the cavity's bounding bipolar lobes increase monotonically in time.

Fast Wind Models: In figure 2, right column, we show the results of Model 2, in which a "classical" fast wind is driven into a spherical AGB wind envelope. The growth of the nebula follows the analytical predictions of Kwok et al. (1978, but see also Stute & Sahai 2006) and agrees well with Schönberner, Jacob, & Steffen (2005), whose 1-D models include much more detailed physics that we could include in our multidimensional models. The slow dense AGB wind is quickly overtaken by the spherical fast wind which is initially 100 times sparser and 20 times faster. An inward facing shock decelerates fast wind gas which is then heated to temperatures of $T \sim 10^7 - 10^8$K; a spherical hot bubble is formed. Such high temperatures have never been observed in PN hot bubbles, and, hence, a number of mechanisms have been proposed to moderate their temperatures (e.g. see Soker et al. 2010, and references therein; Li et al. 2011). The thermal pressure of the hot bubble acts as the piston driving a shock into the AGB envelope. AGB gas swept up by this shock cools rapidly and is compressed into a dense rim expanding with a velocity of $V_{rim} \sim 20\,\mathrm{km\,s^{-1}}$. In this way an isotropically expanding PN is formed, just as described by the simple analytical model of Kwok et al. (1978). The nebula reaches a radius of ~ 0.4 pc after expanding for about 5000 yr.

We note that observations (Bruce Balick 2011, private communication) often find that AGB shells expand with an outward radial gradient (i.e. $v_{AGB} \propto R_{AGB}$). This is not the case in our AGB initial conditions (section 2.1). However, we carried out additional test simulations (not shown) and have found that the morphology results of the present paper do not sensitively depend on the functional form, $v_{AGB} =$ constant vs $v_{AGB} \propto R_{AGB}$, of AGB environments. This happens, in part, because the velocity of the jet and fast wind is faster than v_{AGB} by at least one order of magnitude.

Jet and Fast Wind Models: In figure 3, left column, we show the results of Model 3, in which the collimated jet phase is followed by the spherical fast wind. Initially, the

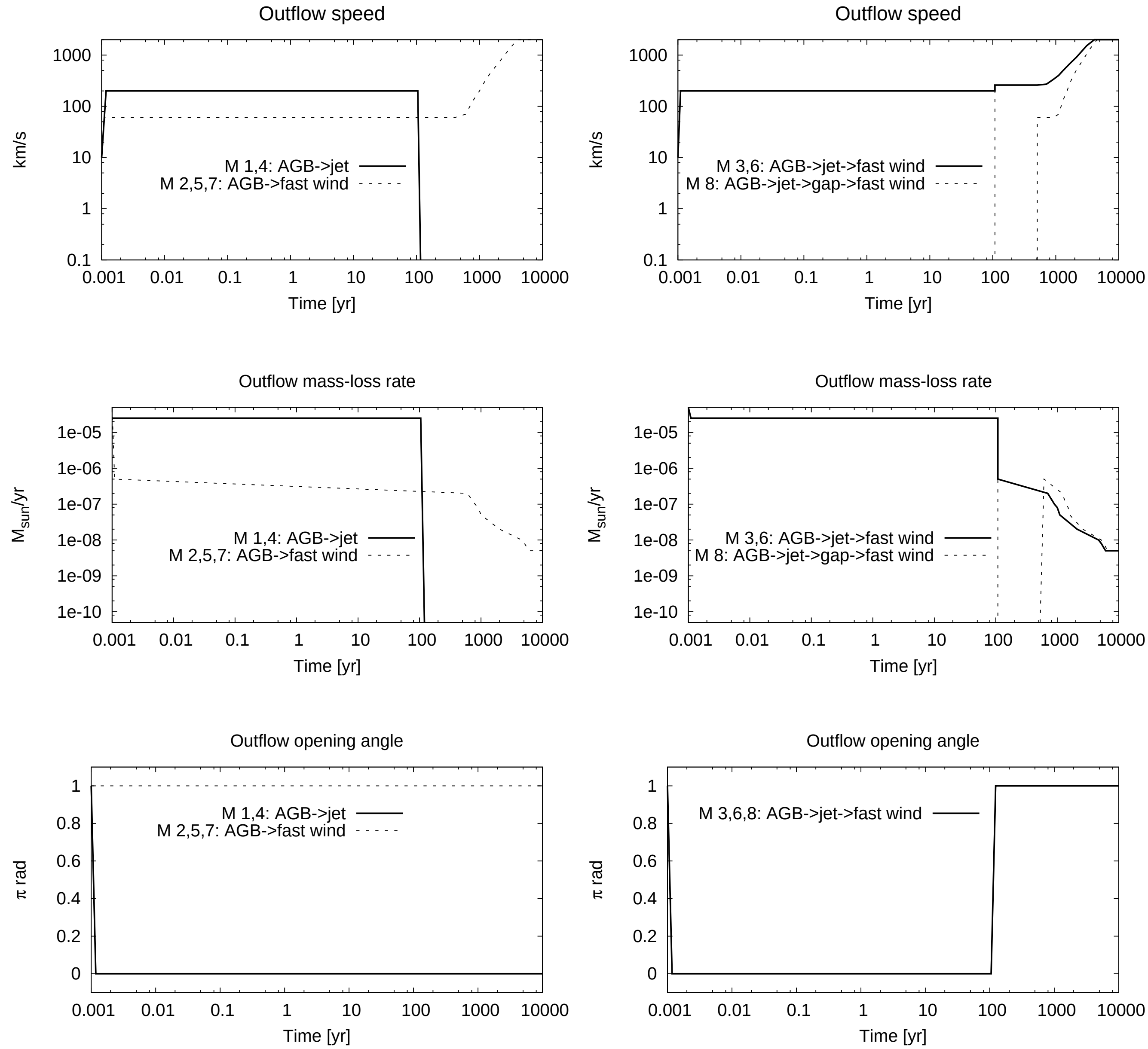

Figure 1. Outflow evolutionary profiles of Models 1-8. The initial conditions (t⩽0.001 yr) are those of the AGB wind and are set throughout the computational domain, whereas the conditions of both jet and fast wind phases are set only on the gas located inside the nozzle. See Table 1 for details.

collimated jet forms a bipolar cocoon at the center of the AGB envelope as in Model 1. Once formed, the jet-driven cavity is then shaped from within by the isotropic fast wind. The fast-wind shock quickly forms, filling the initially bipolar cavity with high temperature gas. The contact surface of the jet-driven cavity is pushed against the slow denser AGB envelope by the internal pressure of the fast wind. Because the jet has already shaped the AGB wind, an elliptical, rather than a spherical, dense rim is eventually formed.

The bubble attains an aspect ratio of ≈ 2 which is achieved early in the evolution and remains roughly constant as the nebula expands. This simulation demonstrates one of the principal points of our study: *An initially bipolar outflow driven by a strongly collimated jet can be transformed into an elliptical nebula at longer times and larger scales by a subsequent isotropic, fast wind.* Thus nebular morphology is not a given of initial conditions but can change over time as the wind driving conditions change.

In most of our models the transition between jet and wind occurs instantly. In Model 8 (figure 5, right column) however, we show the results of a simulation in which we have modified the conditions in Model 3 to include a quiescent period between the jet and the wind. In the evolution of real PN this gap could represent a phase during which energy injection from the CSPN, or binary system, may be absent. As discussed in the previous sections time-scale estimates of such episodes are of order the jet duty cycle, $t \sim 100\,\mathrm{yr}$ (see section 2.1). The simulation shows that, once again, the jet phase leads to the formation of a cavity that is initially bipolar. This fossil structure then expands quasi-ballistically for $\sim 400\,\mathrm{yr}$, reaching scales of order 0.05 pc. The fast wind then begins at time $t = 500\,\mathrm{yr}$, and the evolution of the interacting winds is essentially similar to that of Model 3.

We note that in this simulation the rim of swept up AGB material maintains an aspect ratio close to 2.3 which means that once the fast wind begins the nebula expands homologously (see Figure 6 **and section 4.2).** One difference between this simulation and Model 3 is the late time formation of a dense knot along the long axis of the elliptical rim. The number density and flow speed in the knot are of order $1500\,\mathrm{cm}^{-3}$ and $30\,\mathrm{km\,s}^{-1}$, respectively, which are not unlike those in some FLIERS (see e.g. Balick et al. 1998, and references therein). The formation of the knots appears due to the radiative collapse of jet material as it interacts with the AGB wind. In contrast, when the fast wind immediately follows the jet phase (Model 3) the flux of mechanical energy into the polar regions flattens the jet material and keeps it from forming a ballistically expanding dense knot.

3.2 Structure formation in non-spherical AGB shells

The nebular dynamics changes significantly when the AGB envelope begins with a toroidal density distribution. The results of our studies in this context are summarized in Figure 4. We note that in these models the jet propagates along the symmetry axis of the toroidal AGB envelope.

Jet Model: In figure 3, right column, we show the results of Model 4, in which the jet alone drives into an aspherical AGB wind. Once again the jet drives a fossil bipolar cavity which develops a narrow waist at $\sim 3000\,\mathrm{yr}$ compared to 5000 yr for the spherical AGB shell (of Model 1). The lateral expansion of the lobe is, once again, stronger in lower density regions where the ram pressure of the initial AGB envelope is easier to displace. The lobe that develops in this case has a narrower waist than in models with no pole to equator density contrast. The dynamics of the evolution is, however, not significantly different from the results of Model 1. This means it would be difficult to determine from the morphology of a PPN whether or not the progenitor AGB wind had a significant pole to equator density contrast. Jets, if present, dominate the morphology only if there is no fast wind or if the fast wind has less momentum.

Fast Wind Model: In figure 4, left column, we show the results of Model 5, in which only a fast light isotropic wind interacts with the dense slow toroidal AGB envelope. This is the classic GISW model that has been explored before (e.g. Icke et al. 1992; Frank & Mellema 1994). The Figure shows that, as expected, the swept-up AGB shell becomes elliptical at early times and then becomes more significantly bipolar as the hot bubble drives the shock to larger radii in the AGB wind along the polar axis. At late times the dense rim takes on a butterfly morphology as would be expected for these initial conditions. Thus this simulation and that of Model 2 (spherical AGB wind) recover the results of previous numerical experiments in the GISW and ISW models (e.g. Frank & Mellema 1994) and thereby confirm the consistency of our numerical simulations.

Jet and Fast Wind Model: In figure 4, right column, we show the results of Model 6, in which the jet is followed by the fast isotropic wind as they interact with the toroidal AGB envelope. Once again an initially bipolar cavity and rim are created by the jet. Once the fast wind begins however the evolution differs significantly from Model 3. Rather than changing the morphology from bipolar to elliptical, the action of the fast wind in this case is different; the evolution is dominated not by reshaping the jet driven cavity but by interacting with the toroidal AGB wind. The long term evolution of this model leads to a butterfly shaped rim which is quite similar to that seen in the previous simulation in which no jet was included. *Thus it appears that the presence of a preexisting density contrast in the AGB wind is more important for the evolution of morphology than the presence of a short-lived jet phase as no change from bipolar morphology to elliptical morphology occurs.* We note a large fraction of optical PPN have dense dust waists (see e.g. Huggins 2007, and references therein). Hence the above conclusion would suggest that a large fraction of mature PN should also be bipolar. Since this is not the case it is possible that such dust shells may not be extended enough to influence PN morphology once the fast wind begins.

Asymmetric AGB Velocity: In figure 5, left column, we present Model 7, in which the fast wind expands into an AGB envelope with an aspherical velocity (rather than density) distribution. In our initial conditions the AGB wind expands two times faster toward the pole than towards the equator, following equation (3). The hot bubble responds to the reduced AGB ram pressure $P_{rp}(\theta) = \rho_{AGB} V_{AGB}(\theta)^2$ along the equator leading to high shock velocities at these latitudes. As the figure shows the resulting morphology is elliptical. This simulation demonstrates that if the early evolutionary phase of the PN produce a rapidly expanding *equatorial flow* rather than a *bipolar jet* (Nordhaus et al. 2007), then an elliptical nebula might be the long term result.

3.3 Effect of Ionization Induced Temperature Increase

We note finally that we have compared the evolution of those models with our simple estimate of ionization against the ones with no change in temperature (see Table 1, last column). We find only small changes, of order 5%, in the dynamical behavior of simulations with a temperature increase (from $T \lesssim 500\,\mathrm{K}$ to $T = 10^4\,\mathrm{K}$).

Our models are relevant to cases in which the ionization front remains R-type (see section 2.2) until it leaves the AGB material. We are not able to see details of the ionization front's passage on the gas in terms of driving instabilities which can fragment the dense rim when the fronts stall in the nebular gas. We note that even 1-D models show that the trapping of the ionization can have an effect on the evolution of the rim (Schönberner et al. 2005). These effects should not however affect our conclusions about global changes in morphology. For AGB envelopes that begin with little pole to equator density contrast the trapping of the D-front will occur at all latitudes and its changes will affect the entire rim. Thus ionization effects should not change our conclusions about the morphological shift from bipolar to elliptical nebulae as they will not change the nature of hot

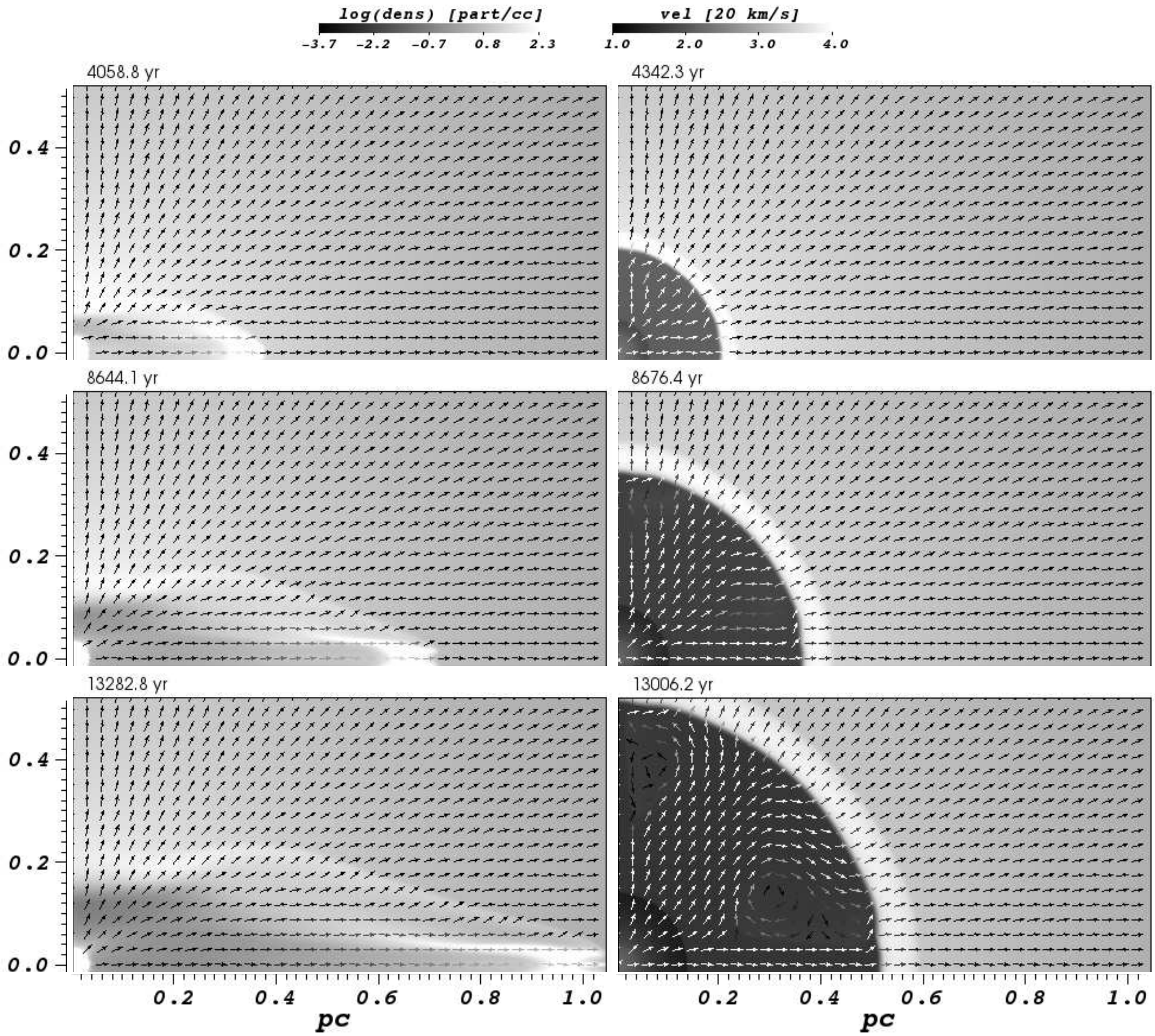

Model 1: spherical AGB wind → jet *Model 2: spherical AGB wind → fast wind*

Figure 2. Dynamical evolution of the gas for different simulations that started with a spherical AGB wind distribution. These are logarithmic false colour grayscale maps of the number density. Columns correspond to different simulations and time increases downwards. Arrows indicate velocity. See Table 1 for details on the model parameters.

bubble pressure gradients driving the rim from the inside. We leave a detailed study on this matter for future work.

4 DISCUSSION

The main results from our simulations are the following. A young bipolar PPN transforms into an older elliptical PN when an initial spherical AGB envelope interacts with a short duration jet and then with a spherical post-AGB fast wind. Once mature PN become elliptical they do not eventually change into more spherical nebulae over relevant time scales. If the initial AGB envelope is toroidal then butterfly nebula occur with or without a PPN jet phase.

4.1 Aspect ratio evolution

We follow the morphological transition of our model nebulae formed from spherical AGB envelopes (Figure 2, Figure 3-left and Figure 5-right) using plots of the rims' aspect ratio, $\epsilon(t) = L_{ma}(t)/L_{mi}(t)$, as a function of time. This is the major-to-minor axis ratio of a rectangle that would contain the principal bright structure of the nebulae. The aspect ratio evolution profiles are shown in Figure 6. It is clear that their gradients are related to the outflow phase sequence, or history, in the simulations.

The spherical PN rim that we see in Model 2 has a constant $\epsilon(t)$ of unity (thick solid line). The bipolar rim in Model 1 has an $\epsilon(t)$ that increases monotonically as the object expands (thin dashed line, Figure 6). The expansion of

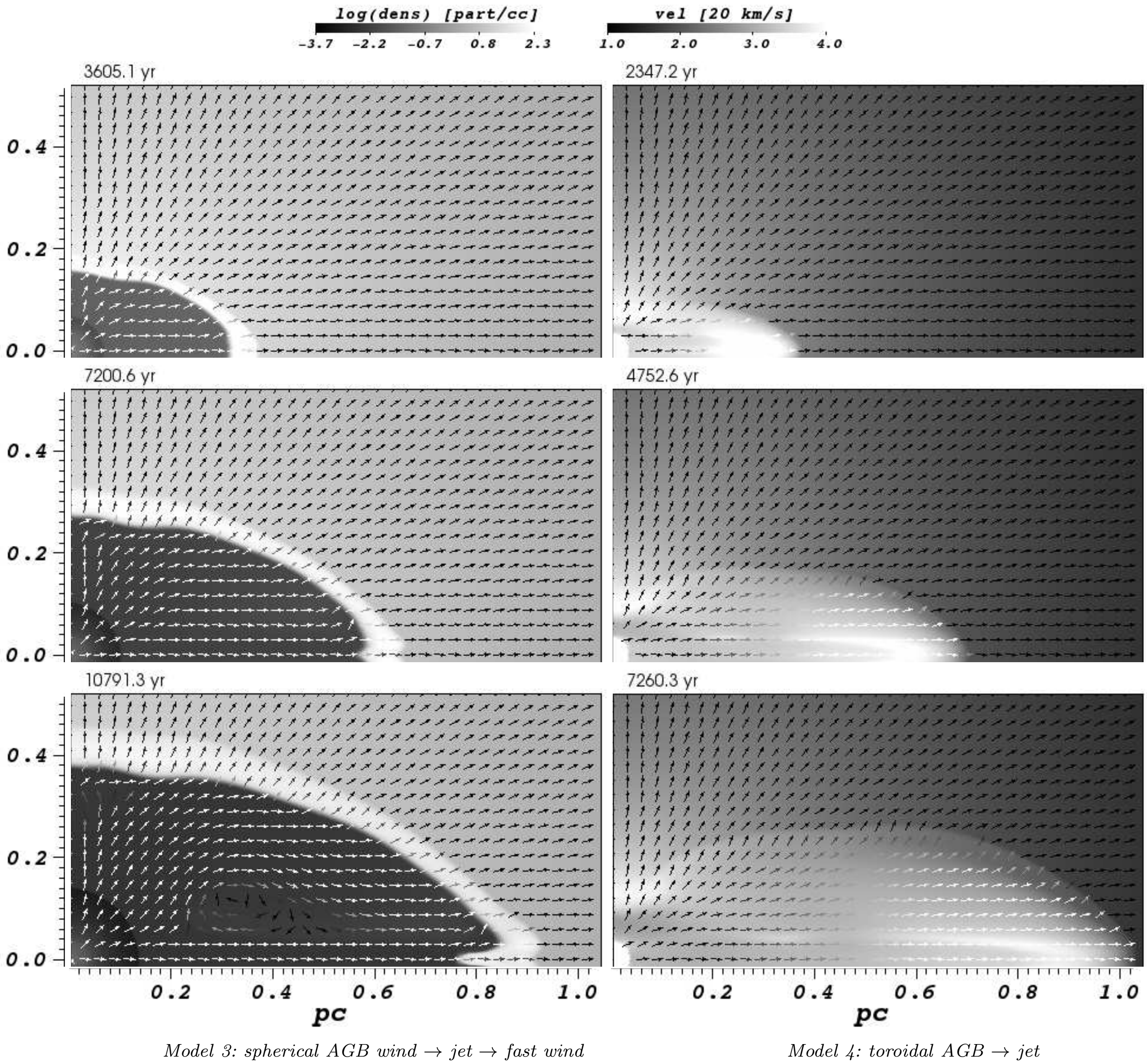

Figure 3. Dynamical evolution of the gas. These are logarithmic false colour grayscale maps of the number density. Columns correspond to different simulations and time increases downwards. Arrows indicate velocity. See Table 1 for details on the model parameters.

this lobe is dominated by the momentum of the jet during the early evolutionary phases, hence we see a steep increase in $\epsilon(t)$. Note that the slope decreases in time because the jet turns off. If the jet were active we would see a constant slope. The aspect ratio of the lobes is (of course) also proportional to the duration of the jet injection phase.

In contrast, the rims in Models 3 and 8 (the thin solid and thick dashed lines in Figure 6, respectively) show quite different evolution of $\epsilon(t)$. For these simulation $\epsilon(t)$ increases steeply during the early evolutionary phases in which the jet dominates the object's expansion. This corresponds to the PPN phase. Any further increase of the aspect ratio is then quickly suppressed by the effects of the spherical fast wind. The profiles reach values of about 2 and vary only modestly afterwards. This means the expansion of the rim becomes homologous **(section 4.2).** This is the most important point of the work.

The thick dashed line corresponds to Model 8 and shows a short increase/decrease in aspect ratio that occurs between the early evolution and the later phases when the aspect ratio becomes constant. This feature occurs during the quiescent evolutionary phase, i.e. the PPN-PN transition. Comparing with the aspect ratio profiles of Models 1 and 3 we see that the height of the bump in Model 8 is proportional to the duration of the quiescent interlude (see end of section 2.1). An interesting question here is that of the dependence of $\epsilon(t)$ on the duration of this interlude. To answer this, additional simulations (designed to explore a set of values for the duration of the interlude) would have to be carried out; we leave this for future research.

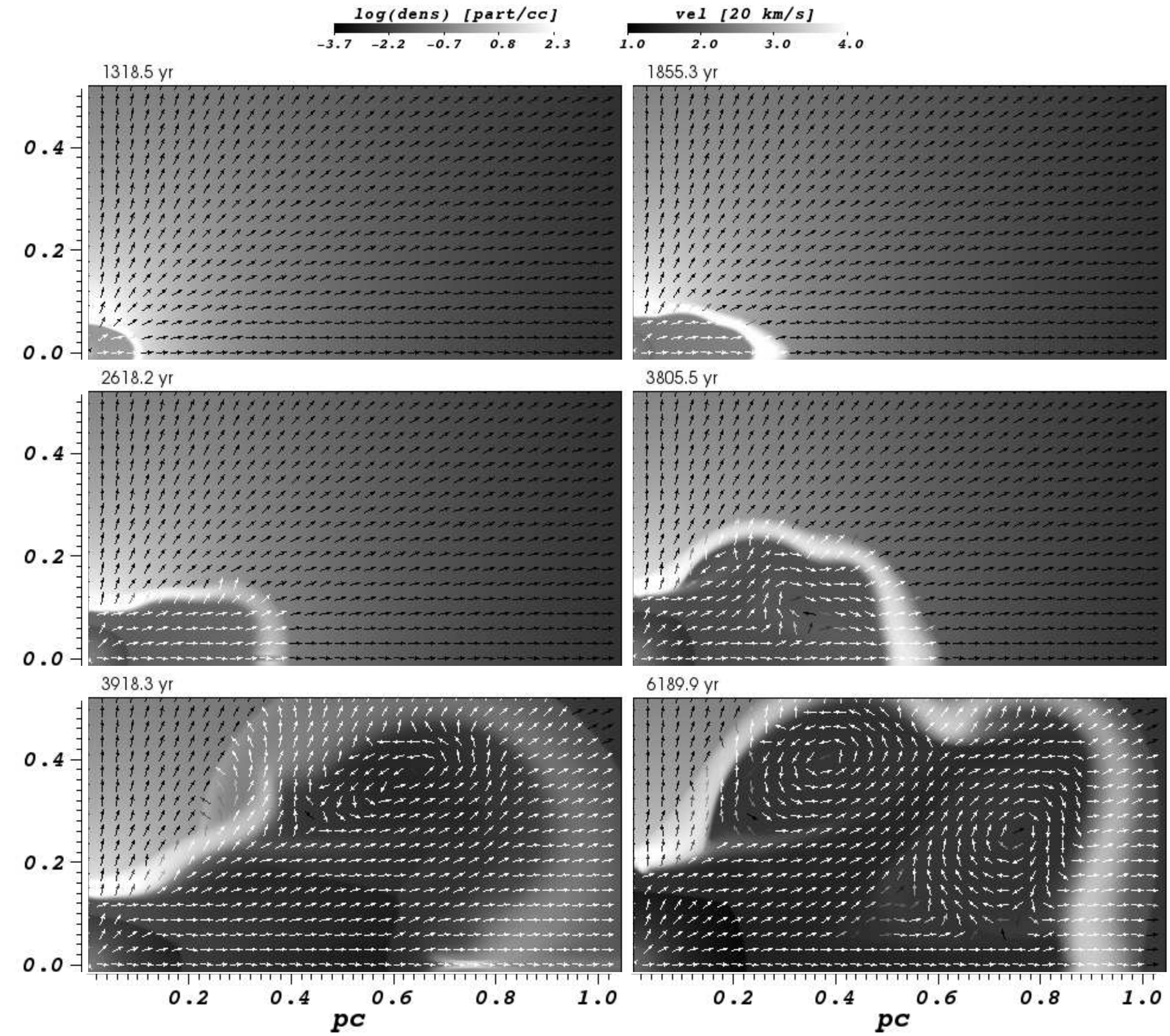

Model 5: toroidal AGB → fast wind *Model 6: toroidal AGB → jet → fast wind*

Figure 4. Dynamical evolution of the gas for different simulations that started with a toroidal AGB wind density distribution.These are logarithmic false colour grayscale maps of the number density. Columns correspond to different simulations and time increases downwards. Arrows indicate velocity. See Table 1 for details on the model parameters.

Our calculations therefore demonstrate how the morphology of PPN and PN is correlated with the collimation parameters of the wind from the central object. The presence of a brief, hypersonic and heavy jet prior to the interaction between the AGB envelope and the spherical fast wind changes the shape of the resulting nebulae. The effects are important during both the early and late phases of nebular expansion. Bipolar PPN are formed and then turn into elliptical PN, in broad agreement with the general statistical trends of the observed morphologies of PN.

4.2 Velocity field

We show the velocity field of gas in our simulations in Figures 2, 3, 4 and 5. Vector density, location and length are constant, but vector inclination and grey scale are related to the local direction and speed of the flow, respectively. Arrow properties were chosen in such a way as to stress velocity differences between the polar and equatorial parts of our model nebular rims. A detailed study of the velocity field distribution of material inside the lobes, as well as in butterfly-shaped rims, is beyond the scope of this paper.

The following findings are consistent with the nebular aspect ratio evolution profiles of Figure 6.

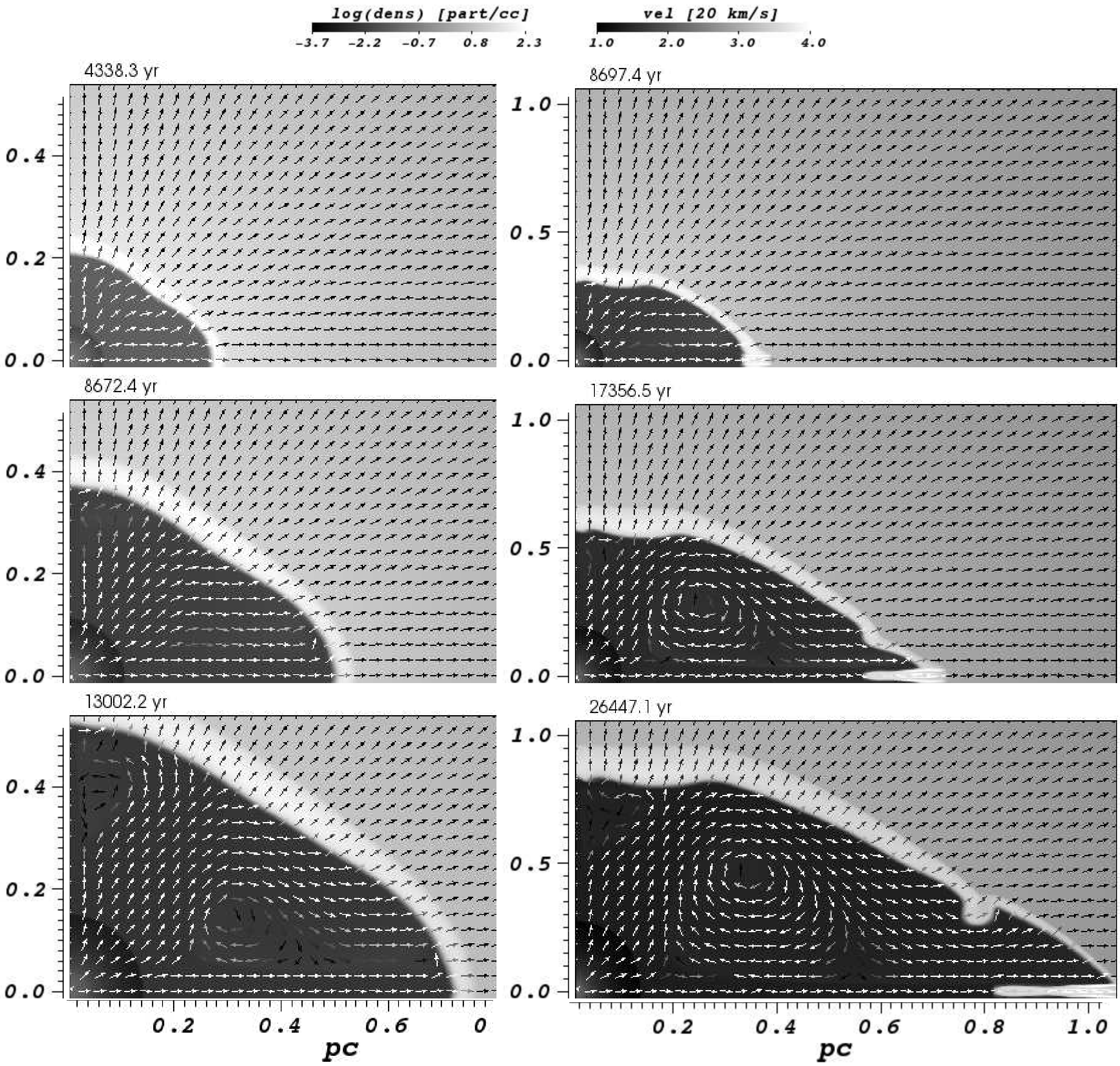

Model 7: aspherical AGB velocity → fast wind *Model 8: spherical AGB wind → jet → no outflow for ∼400 yr → fast wind*

Figure 5. Dynamical evolution of the gas. These are logarithmic false colour grayscale maps of the number density. Columns correspond to different simulations and time increases downwards. Arrows indicate velocity. See Table 1 for details on the model parameters.

The left column of Figure 2 shows that the tip of the bipolar rim formed in Model 1 maintains a longitudinal (horizontal) velocity, v_z, which is close to $75\,\mathrm{km\,s^{-1}}$. Lobe material located behind the tip shows a v_z increase proportional to the distance from the star, z. This is consistent with the "Hubble flow" kinematics observed in some PPN outflows (Balick & Frank 2002; Bujarrabal et al. 1998; Olofsson & Nyman 1999). In contrast, the velocity of the rim's waist (Figure 2, left) is mostly transverse, v_r, slower (darker) and quite similar to that of the AGB wind material located at larger radii. We see a similar velocity distribution at the tip and waist of the bipolar rim formed in Model 4 (Figure 3, right column). I.e. a fast (light-gray) tip with $v_r, v_z \sim 0{,}100\,\mathrm{km\,s^{-1}}$, and a slower (dark-gray) waist with $v_r, v_z \sim 20{,}0\,\mathrm{km\,s^{-1}}$. In this case however most of the lobe material, not just the component behind the rim's tip, also shows a v_z increase proportional to the distance from the star.

The left column of Figure 3 shows that the elliptical PN rim of Model 3 has a consistent, progressive speed increase (dark to light gray) of a factor ~ 2, form the waist to the tip along the rim. This velocity

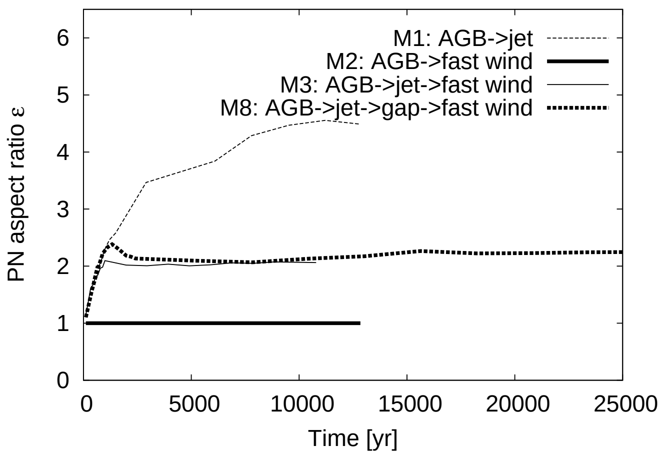

Figure 6. Time evolution of the nebular aspect ratio, $\epsilon(t)$. The $y-$axis shows the major-to-minor axis ratio of the rims (the principal bright structures). Profile gradients correlate with the outflow phase sequence, or history.

field goes from transversely dominated at small z to longitudinally dominated at large z. The object expands homologously. In this case we do not see any correlation between the position on the z-axis and the speed of the lobe material. We see similar velocity distributions in the elliptical PN rims of Models 7 and 8 (Figure 5). The tip-to-waist speed ratio $[v_z(r=0)/v_r(z=0)]$ of the rims in Models 7 and 8 is $\sim$1.5 and 2, respectively. Also, we consistently find velocity vortices inside the lobes of our model elliptical PN. It is worth noting the semi-analytical kinematic analysis of Steffen et al. (2011) which suggests that in general PN rims asymptotically evolve towards a homologous expansion, in agreement with our findings.

4.3 Synthetic observations

The simulations described in section 3 yield detailed predictions of the density structures of PN (as well as their detailed, if simplified, temperature structures) that, in principle, can be used to generate synthesized emission maps for comparison with the main observed PN morphologies across the electromagnetic spectrum. As a first step in this direction, we synthesized emission measure distribution images (i.e. the integral of ρ^2 along the line of sight) for Models 1, 2, 3 and 8 using the reconstruction tool *Shape* (Steffen & López 2006) and following the procedure described by Steffen et al. (2009). We choose these models because their shapes depend only on their outflow histories. We use logarithmic grayscales and an inclination of 90° between the polar axis of the nebulae and the line of sight (edge-on). Note that in constructing these maps, we have not attempted to account for spatial variations in gas temperature or ionization state; because much of the gas in these simulations is at time average mean temperatures of order 10^4 K, the synthetic images in Figure 7 likely best approximate the appearances the nebulae would have in optical emission lines (e.g., reflected starlight, emission lines arising in shocks and recombination lines). A more detailed, multiwavelength treatment of the synthesized emission morphologies, which is beyond the scope of this paper, will be the subject of future work.

With the above caveats in mind, these initial synthesized emission maps illustrate the clear relationship between the emission morphology of a PN and its CSPN outflow history (i.e. collimated jet or isotropic fast wind). A bipolar object is formed by the interaction of a dense slow AGB envelope with a brief phase of collimated heavy jet ejection (Model 1, Figure 7). The interaction of a light isotropic fast wind with a spherical AGB envelope yields a spherical nebula (as in Model 2 as well). The PN rim in these cases shows an emission distribution with a smooth interior surface brightness and limb-brightened edges.

When all three outflow phases are present, on the other hand, we see young (not-narrow-waisted) bipolar nebulae (Models 3 and 8, top row, Figure 7) transformed into older larger elliptical nebulae (bottom row). The process is particularly evident in Model 8 and affirms the behavior seen in the aspect ratio profiles (Figure 6). Such morphological transition is consistent with the general trends found by observational studies.

The elliptical rims in cases 3 and 8 have similar morphologies. However, their synthetic emission during the PN phase is significantly affected by the presence of the quiescent episode simulated only in Model 8. Figure 7 (bottom) shows that the nebula in Model 3 has an emission distribution with only modest variation in brightness along the rim. In contrast, the PN nebula in Model 8 shows two bright knots along its polar axis, located symmetrically with respect to the center. Examination of the simulation data shows a density contrast of order 100 between the main part of the nebula and the bright knots. It is noteworthy that these features bear some morphological resemblance to the FLIERS that are seen in some elliptical PN (see end of section 3.1).

4.4 PPN/PN morphological changes and progenitor stars

It has been suggested that the outflow mass-loss properties of PN, in particular their geometry, are affected by both the characteristics and multiplicity of their progenitor stars (Iben 1991; Livio 1993; Soker 1997; Soker 1998, and references therein; Nordhaus & Blackman 2006; Nordhaus et al. 2007; De Marco 2009; De Marco & Soker 2011). Where do our models fit in this picture? In other words, which binaries are expected to produce both spherical AGB envelopes and jets which could then lead to the morphological change we see in Models 3 and 8 (from bipolar to elliptical)?

Although we have a reasonable understanding of how dust-driven winds can explain the high mass-loss rates observed during the AGB superwind phase (e.g. Morris 1987; Lagadec & Zijlstra 2008) questions remain open, in particular regarding the geometry change that must take place during the AGB-to-PPN transition. Today, it appears unlikely that a single star may power the evolution of an AGB star that results in a non-spherical PN (e.g. Nordhaus et al. 2007), although it is possible that in the future we may understand how a dynamo could be sustained in an AGB star and generate a super-wind phase that departs from spherical symmetry (Blackman et al. 2001). The type of binary

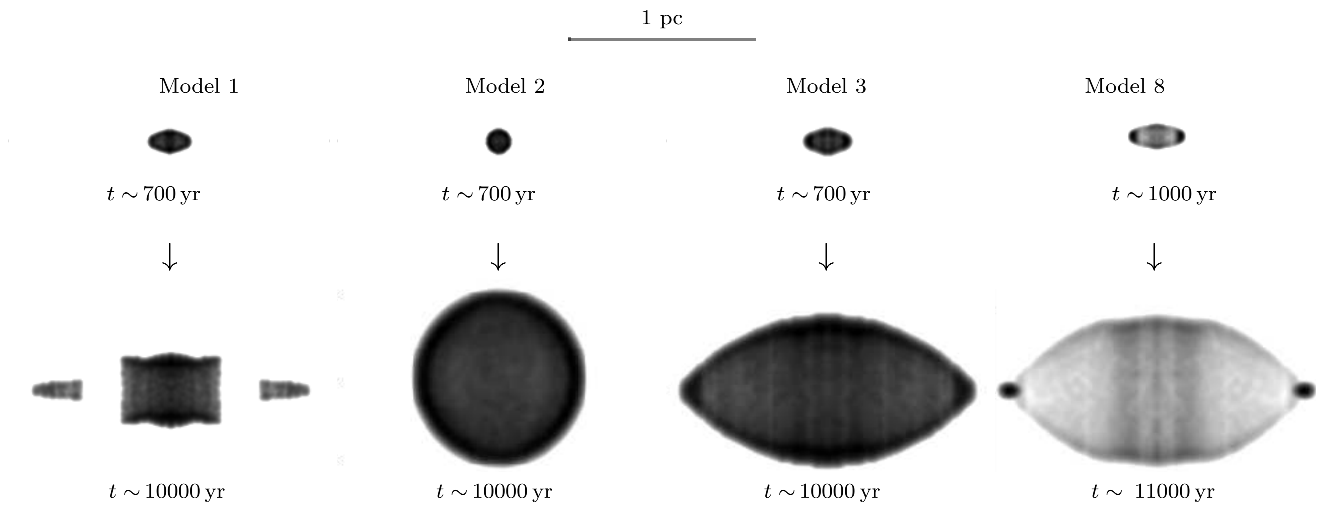

Figure 7. Synthetic emission maps of the model nebulae. The inclination angle of the images is 90°. These are emission measure distribution images (i.e. the integral of ρ^2 along the line of sight) produced using Shape (Steffen & López 2006). Grayscales are logarithmic.

that could give rise to the simulated ejection phases can be surmised from basic physical arguments and simulations.

Companions that are located within 2-3 AGB star radii can be captured into a common envelope (Nordhaus et al. 2010). The subsequent in-spiral causes the AGB envelope to be ejected (likely in a toroidal geometry; Sandquist et al. 1998) and the post-AGB star to emerge with a much reduced radius and much higher temperature. Observed systems (e.g., De Marco 2009) and simulations (e.g., Sandquist et al. 1998, Ricker and Taam 2008, Passy et al. 2011) indicate that the post-common envelope primary will be a star with a radius within a solar radius and may bypass the PPN phase altogether, emerging primarily as a bipolar PN (although some post-common envelope PN are actually elliptical; Miszalski et al. 2009a,b). It is not clear whether a jet would ensue, although highly collimated structures are observed in post-common envelope PN (e.g., Abell 63; Mitchell et al. 2007).

For some post-CE PN with jets, the jet is kinematically older than the main PN and may have started before the bulk of the envelope departed the system (e.g. A63, Mitchell et al. 2007) or ETHOS 1 (Miszalski et al. 2011). For these cases Models 4, 5 or 6 may be fitting. In at least one case, however, this is the other way around and the jet is younger than the PN (NGC6 778, Guerrero & Miranda 2012).

A class of binaries exists that has larger final separations (100-500 $R_{\odot}$; van Winckel 2003; van Winckel et al. 2009). It is unknown if a common envelope resulted in their formation. Such post-AGB primaries are almost never accompanied by a PPN. In a couple of instances bipolar outflows are seen (e.g., the Red Rectangle; Cohen et al. 2004, and references therein). We note that circumbinary disks are observed around all of these system. These binaries may never develop a proper PN due to their envelope being replenished by fall-back of disk material, which could prevent a temperature increase of the central star. It is not clear if any of our models might mimic this evolutionary channel.

Other binary types that could fit our models can be wider binaries, those with initial separations larger than a few stellar radii (5-10 AU). These can focus the AGB wind into an equatorially concentrated torus (Edgar et al. 2008), accrete matter and blow jets either before or after AGB departure. Any of our models could simulate such scenario. If the companion is lower mass, both the focussing action and the jet blowing may be weak. The star might evolve as if single then.

If a companion is captured tidally by an AGB star *and* it has considerable mass (larger than a few tenths of a solar mass), it will synchronise the AGB stellar rotation with the orbital motion (Counselman 1973). When this happens the AGB star is spun up and may eject an equatorially concentrated wind. A common envelope would be avoided because the tidal capture would be slowed down. Jets may be blown for a period during or after the AGB envelope ejection. An example of this scenario could be Model 6.

Finally, if a companion caught into a common envelope is low mass (such as a brown dwarf or even less massive) and tidally destroyed within the common envelope, it may form a disk around the core and blow jets. In this scenario a jet may precede a possibly toroidal AGB wind.

5 CONCLUSIONS AND SUMMARY

We have carried out a series of 2.5D hydro simulations designed to study how changing the mass-loss properties of PN progenitor stars affects the evolution of nebular morphology. The stellar mass-loss evolution has been followed starting at the AGB phase, evolving through the PPN phase and finishing at the mature PN phase.

Our simulations show that a young bipolar PPN transforms into an older elliptical PN when an initially spherical AGB envelope interacts with a short duration jet, driven from the central star and followed by an isotropic fast wind.

Thus we have demonstrated how changing mass-loss geometries from the central engine can drive evolutionary changes in nebular morphology. Our theoretical results complement GISW studies. A fast spherical CSPN wind driving into a slow spherical AGB wind has been thought to create a spherical nebula. We have shown that if this interaction is preceded by a collimated PPN jet phase then an elliptical PN will result. A fast spherical CSPN wind driving into a slow aspherical AGB wind has been thought to create an aspherical nebula and our results show that including an earlier PPN jet phase does not affect the eventual butterfly morphology that results.

Our theoretical result that bipolar PPN can evolve into elliptical PN is consistent with general observational trends suggesting that PPN appear to favor bipolar morphologies while mature PN appear to be more elliptical. This result has to be considered along side of the complementary observational trend that bipolar PN are found at typically lower Galactic scale heights than ellipticals, suggesting a correlation between bipolarity and higher-mass (shorter lifetime) progenitors (Corradi & Schwarz 1995; Kastner et al. 1996; Manchado et al. 2011).

We also have found that once mature PN become elliptical they do not evolve to become spherical nebulae over the relevant PN lifetimes, so the origin of mature spherical PN (19% of all PN; Parker et al. 2006; Miszalski et al. 2008) does not seem to follow the initially aspherical pathway studied herein.

The aspect ratio evolution of our model nebulae suggests that bipolar PN with projected aspect ratios $\gtrsim 4$ may result from CSPN which during the post-AGB phase develop a brief jet, but no fast spherical winds, or relatively weak ones (e.g., symbiotic Mira systems like R Aqr, Mz 3, Belczyński et al. 2000, and references therein; Mz 3, Schwarz et al. 1992).

When the initial jet drives into a toriodal AGB density distribution the result is a bipolar PPN that evolves into a mature bipolar nebula with a narrow waist. The toroidal AGB density distribution in this case dominates the dynamics and shape of any subsequent outflow phases. At late times the asymptotic geometry of this nebula is a traditional butterfly nebula when seen in projection onto the sky. We also find that the interaction of a spherical post-AGB fast wind with an AGB envelope which has an aspherical velocity field yields a homologously expanding elliptical nebula.

One of our simulations included a quiescent interlude between the jet and the fast wind episodes. We find the corresponding synthetic emission map shows small bright features which resemble observations of axial knots or FLIERS within PN. A future avenue for these studies would be to explore when and how knots form as the result of jet material collecting at the head of the flow.

ACKNOWLEDGMENTS

Financial support for this project was provided by the Space Telescope Science Institute grants HST-AR-11251.01-A and HST-AR-12128.01-A; by the National Science Foundation under award AST-0807363; by the Department of Energy under award DE-SC0001063 and by Cornell University grant 41843-7012. JHK acknowledges financial support by award number GO1-12025A issued to RIT by the Chandra X-ray Observatory Center, which is operated by the Smithsonian Astrophysical Observatory for and on behalf of NASA under contract NAS8-03060. MHE thanks Jonathan Carroll for discussions. **We thank the referee, Wolfgang Steffen, for useful comments that helped to improve this paper.**

REFERENCES

Akashi, M., Soker, N., 2008, MNRAS, 391, 1063
Balick B., 1987, AJ, 94, 671
Balick, B., Alexander, J., Hajian, A. R., Terzian, Y., Perinotto, M., Patriarchi, P., 1998, AJ, 116, 360
Balick B., Frank A., 2002, ARA&A, 40, 439
Belczyński, K., Mikołajewska, J., Munari, U., Ivison, R. J., Friedjung, M., 2000, AAPS, 146, 407
Bujarrabal, V., Castro-Carrizo, A., Alcolea, J., Sánchez Contreras, C., 2001, AAP, 377, 868
Corradi, R. L. M., et al., 2011, MNRAS, 410, 1349
Castro-Carrizo, A., 2007, Asymmetrical Planetary Nebulae IV
Cohen, M., Van Winckel, H., Bond, H. E., Gull, T. R., 2004, Aj, 127, 2362
Corradi, R. L. M., Schwarz, H. E., 1995, AAP, 293, 871
Counselman, C. C., III 1973, ApJ, 180, 307
Cunningham A. J., Frank A., Varnière P., Mitran S., Jones T. W., 2009, ApJS, 182, 519
Dalgarno A., McCray R. A., 1972, ARA&A, 10, 375
De Marco, O., Sandquist, E. L., Mac Low, M.-M., Herwig, F., Taam, R. E., 2003, Revista Mexicana de Astronomia y Astrofisica Conference Series, 18, 24
De Marco, O., 2009, PASP, 121, 316
De Marco, O., & Soker, N., 2011, arXiv:1102.4647
Edgar, R. G., Nordhaus, J., Blackman, E. G., Frank, A., 2008, ApJL, 675, L101
Frank A., Mellema G., 1994, ApJ, 430, 800
García-Arredondo, F., Frank, A., 2004, ApJ, 600, 992
Giuliani, J. L., Jr., 1981, ApJ, 245, 903
Groenewegen, M. A. T., 1996, AAP, 305, L61
Guerrero, M. A., & Miranda, L. F., 2012, arXiv:1201.2042
Hartigan, P., Frank, A., Varniére, P., Blackman, E. G., 2007, ApJ, 661, 910
Hollenbach D. J., Tielens A. G. G. M., 1997, ARA&A, 35, 179
Huggins P. J., 2007, ApJ, 663, 342
Iben, I., Jr., 1991, ApJs, 76, 55
Icke, V., 1988, AAP, 202, 177
Icke, V., Balick, B., Frank, A., 1992, AAP, 253, 224
Jacoby, G., Ferland, G. J., Korista, K. T., 2000, Bulletin of the American Astronomical Society, 197, 616
Kastner, J. H., Weintraub, D. A., Gatley, I., Merrill, K. M., Probst, R. G., 1996, ApJ, 462, 777
Kastner, J. H., Montez, R., Jr., Balick, B., De Marco, O., 2008, ApJ, 672, 957
Knapp, G. R., Morris, M., 1985, ApJ, 292, 640
Kwok S., Purton C. R., Fitzgerald P. M., 1978, ApJ, 219, L125
Lagadec, E., Zijlstra, A. A., 2008, MNRAS, 390, L59
Lagadec, E., et al., 2011, arXiv:1102.4561
Lee, C.-F., Sahai, R., 2003, ApJ, 586, 319
Lee, C.-F., Sahai, R., 2004, ApJ, 606, 483
Lee, C.-F., Hsu, M.-C., Sahai, R., 2009, ApJ, 696, 1630
Li, S., Frank, A., & Blackman, E., 2011, arXiv:1110.0817
Livio, M., 1993, Planetary Nebulae, 155, 279

Manchado, A., Garcia-Hernandez, D. A., Villaver, E., Guironnet de Massas, J., 2011, arXiv:1106.5751
Miszalski, B., Parker, Q. A., Acker, A., Birkby, J. L., Frew, D. J., Kovacevic, A., 2008, MNRAS, 384, 525
Miszalski, B., Acker, A., Moffat, A. F. J., Parker, Q. A., Udalski, A., 2009, AAP, 496, 813
Miszalski, B., Acker, A., Parker, Q. A., Moffat, A. F. J., 2009, AAP, 505, 249
Miszalski, B., Corradi, R. L. M., Boffin, H. M. J., Jones, D., Sabin, L., Santander-García, M., Rodríguez-Gil, P., Rubio-Díez, M. M., 2011, MNRAS, 413, 1264
Miszalski, B., Jones, D., Rodríguez-Gil, P., Boffin, H. M. J., Corradi, R. L. M., Santander-García, M., 2011, AAP, 531, A158
Mitchell, D. L., Pollacco, D., O'Brien, T. J., Bryce, M., López, J. A., Meaburn, J., Vaytet, N. M. H., 2007, MNRAS, 374, 1404
Morris, M., 1987, PASP, 99, 1115
Nordhaus, J., Blackman, E. G., 2006, MNRAS, 370, 2004
Nordhaus J., Blackman E. G., Frank A., 2007, MNRAS, 376, 599
Nordhaus, J., Spiegel, D. S., Ibgui, L., Goodman, J., Burrows, A., 2010, MNRAS, 408, 631
Olofsson, H., & Nyman, L.-Å., 1999, AAP 347, 194
Parker, Q. A., et al., 2006, MNRAS, 373, 79
Passy, J.-C., Fryer, C. L., Diehl, S., De Marco, O., Mac Low, M., Herwig, F., Oishi, J. S., 2011, Bulletin of the American Astronomical Society, 43, #144.18
Passy, J.-C., De Marco, O., Fryer, C. L., et al., 2012, ApJ, 744, 52
Perinotto M., Schönberner D., Steffen M., Calonaci C., 2004, A&A, 414, 993
Ricker, P. M., Taam, R. E., 2008, ApJL, 672, L41
Stute, M., Sahai, R., 2006, ApJ, 651, 882
Sahai, R., Morris, M. R., Villar, G. G., 2011, AJ, 141, 134
Sahai, R., Trauger, J. T., 1998, AJ, 116, 1357
Sandquist, E. L., Taam, R. E., Chen, X., Bodenheimer, P., Burkert, A., 1998, ApJ, 500, 909
Schönberner, D., Jacob, R., & Steffen, M., 2005, AAP, 441, 573
Schwarz H. E., Corradi R. L. M., Melnick J., 1992, A&AS, 96, 23
Soker, N., 1990, AJ, 99, 1869
Soker, N., 1996, ApJ, 468, 774
Soker, N., 1997, ApJS, 112, 487
Soker, N., 1998, ApJ, 496, 833
Soker, N., Rahin, R., Behar, E., Kastner, J. H., 2010, ApJ, 725, 1910
Stanek, K. Z., Knapp, G. R., Young, K., Phillips, T. G., 1995, ApJS, 100, 169
Steffen, W., Martínez, S., & López, J. A., 2011, Asymmetric Planetary Nebulae 5 conference, held in Bowness-on-Windermere, U.K., 20 - 25 June 2010, A. A. Zijlstra, F. Lykou, I. McDonald, and E. Lagadec, eds. (2011) Jodrell Bank Centre for Astrophysics
Steffen, W., López, J. A., 2006, RMxAA, 42, 99
Steffen, W., García-Segura, G., Koning, N., 2009, ApJ, 691, 696
van Winckel, H., 2003, ARAA, 41, 391
van Winckel, H., et al., 2009, AAP, 505, 1221

This paper has been typeset from a TEX/ LATEX file prepared by the author.